



# Ultrabroad-band and low-frequency microwave absorption based on activated waxberry metamaterial

Xianxian Sun<sup>a,b</sup>, Zhuo Wang<sup>c</sup>, Shasha Wang<sup>a,b</sup>, Yuanhao Ning<sup>a,b</sup>, Minglong Yang<sup>a,b</sup>,  
Shuang Yang<sup>a,b</sup>, Lei Zhou<sup>c</sup>, Qiong He<sup>c</sup>, Yibin Li<sup>a,b,d,\*</sup>

<sup>a</sup> National Key Laboratory of Science and Technology on Advanced Composites in Special Environments, Harbin Institute of Technology, Harbin 150080, PR China

<sup>b</sup> Center for Composite Materials and Structures, Harbin Institute of Technology, Harbin 150080, PR China

<sup>c</sup> State Key Laboratory of Surface Physics and Key Laboratory of Micro and Nano Photonic Structures (Ministry of Education) and Department of Physics, Fudan University, Shanghai 200438, PR China

<sup>d</sup> Shenzhen STRONG Advanced Materials Institute Ltd. Corp, Shenzhen 518000, PR China

## ARTICLE INFO

### Keywords:

Activated waxberry  
Metamaterial  
Ultrabroad band  
Microwave absorption  
Low frequency

## ABSTRACT

Low-frequency yet ultrabroad band microwave absorption still remains a great challenge due to contradiction between impedance match and electromagnetic loss. The natural biomass with hierarchical structure provides new solution to address this issue. The electromagnetic (EM) metamaterials show frequency-designable advantage while its absorption band width is often limited. Here we report an alternative EM metamaterial based on activated waxberry with gradient impedance profile. Strong microwave absorptions at low frequencies were experimentally realized with our fabricated metamaterial, achieving  $< -10$  dB reflection loss at 1–4 GHz. Moreover, ultrabroad band feature is achieved with effective absorbing band (reflection loss  $\leq -10$  dB) covering from 1 to 40 GHz. In addition, our meta-design exhibits nearly incident-angle independent property (from 5 to 40°) on the microwave absorption. The excellent performance of our low-frequency meta-absorber is attributed to the excellent interface impedance match of meta-structure and the high dielectric loss due to chemical activation. The broad band absorption is due to the gradient radial microstructure of carbonized waxberry. Our new metamaterial is very promising in the electromagnetic shielding application especially at low frequency.

## 1. Introduction

To address the ever-increasing electromagnetic (EM) pollution caused by rapid development of electronic technology, tremendous effort has been devoted to develop high-performance microwave absorbers [1]. In general, stringent requirements for microwave absorbers such as lightweight, high-strength, and broader qualified absorption bandwidth (reflection loss, RL, below  $-10$  dB) are necessary [2]. Recently, the low-frequency microwave absorption (MA) is extraordinarily required. Designable electromagnetic metamaterial offers strong low-frequency MA property [3–5] while it is difficult to achieve wide band [6]. On the other hand, it is very exciting that carbonized biomass with hierarchical structure shows the ultrabroad band wave absorption property [7–10]. Nevertheless, these carbonized biomass did not exhibit excellent MA property at low frequency, particularly in 1–4 GHz [2]. Low-frequency yet ultrabroad band MA still remains a great challenge.

Recently, macroscopic periodic structure microwave absorbers have showed excellent MA properties (4–40 GHz) [11–15]. Usually, magnetic materials were utilized to promote the low-frequency MA and polymers were served as supporting materials in real structure fabrication process. However the relatively high (over  $1 \text{ g cm}^{-3}$ ) density of absorbers [16–18] largely limited its application in areas requiring lightweight, such as aerospace. Moreover, qualified MA in the frequency range of 1–40 GHz has not been reported at present, even with a large proportion of magnetic materials [19–23]. Our previous work [24] found that carbonized waxberries (CW) exhibit excellent MA properties owing to the unique hierarchical structure with low density and qualified reaching to 32 GHz (8–40 GHz). Nevertheless, the MA performance is unsatisfactory (the RL is only  $-8$  dB) in the frequency range of 1–8 GHz. In order to achieve low frequency yet ultrabroad band microwave absorption, here we propose the activation strategy to tune the dielectric constant, interface polarization loss and dipole polarization loss in order

\* Corresponding author at: National Key Laboratory of Science and Technology on Advanced Composites in Special Environments, Harbin Institute of Technology, Harbin 150080, PR China.

E-mail address: [liyibin@hit.edu.cn](mailto:liyibin@hit.edu.cn) (Y. Li).

<https://doi.org/10.1016/j.cej.2021.130142>

Received 4 March 2021; Received in revised form 17 April 2021; Accepted 24 April 2021

Available online 2 May 2021

1385-8947/© 2021 Elsevier B.V. All rights reserved.

to meet the low frequency wave absorption requirement. At the same time, we adopt the metamaterial strategy based on spherical and hemispherical activated CW (ACW) in order to meet the wave impedance match and ultrabroad band MA requirements. The absorber (named as M-ACW) shows ultralow-frequency yet ultrabroad band MA performance. The effective absorption band could cover 1–40 GHz even with the incident angel changing from 5° to 40°, which shows promising application in the field of electromagnetic shielding especially at low frequency yet ultrabroad band.

## 2. Results and discussion

The preparation procedure of M-ACW is schematically shown in Fig. 1. Firstly, fresh waxberries were freeze-dried and then carbonized at 700 °C using the method reported previously [24]. The obtained CW was immersed in KOH solution by vacuum assisted method. Mapping images of K elements in the outer structure and nucleus confirmed that KOH has been completely immersed into the CW and K become distinctly dense with the increase of KOH concentration (see Fig. S1 in Supporting Information). The ACW was obtained by heating up CW@KOH in argon atmosphere at 600–750 °C. In the process, KOH gradually reacted with carbon as temperature increases, releasing gas and producing some oxygen-containing functional groups. The hemispherical ACW-700 samples (Fig. S2, Supporting Information) could be obtained by cutting the waxberries in half from the middle before freeze drying. As shown in Fig. 1, M-ACW can be considered as microwave metamaterial realized by periodically arranging the whole sphere and hemisphere activated waxberries. Here, the periodicity of M-ACW can be tuned through changing the number of waxberries in a fixed size acrylic sheet.

In order to study the effect of activation on CW, the microstructure and chemical states of samples before and after activation were systematically analyzed (Fig. 2). Compared to unactivated CW [24], the outer layer (named as morning glory-like structure) of ACM retains multi-scale hollow tubular structure with diameters ranging from several microns to hundreds of microns (Fig. 2a). It is worth highlighting that many holes with a diameter of tens of micron in the wall (the area solid red line marked) were found in the activated sample, which was caused by the violent reaction between carbon and KOH. And the inner layer is the hollow core with a porous wall (Fig. S3, Supporting

Information), the same as the ones before activation. The high-resolution transmission electron microscopy (HRTEM) image shows that morning glory-like structure and core from ACW-700 are mainly composed of amorphous carbon, in which some carbon nanocrystalline is embedded (Fig. 2b and Fig. S3 a2–a3, Supporting Information). Whereas, no microcrystalline carbon was found in the CW samples, indicating that the activation process of KOH induced the formation of microcrystalline [25]. Two broad diffraction peaks centered at 24.3° and 43.3° can be observed in X-ray diffraction (XRD) pattern of morning glory-like structure and core structure (Fig. 2c and Fig. S3d, Supporting Information), confirming the existence of disordered graphitic carbon. The densities of CW and ACW were measured by mass over volume. As revealed in Fig. 2d, the density of morning glory-like structure decreased by 50% (from 0.1 g cm<sup>-3</sup> to 0.05 g cm<sup>-3</sup>) after activation. Meanwhile, the density of core's wall reduced from 0.94 g cm<sup>-3</sup> to 0.678 g cm<sup>-3</sup>. Accordingly, the total density changed from 0.13 g cm<sup>-3</sup> to 0.088 g cm<sup>-3</sup> after activation due to carbon reduction. Amazingly, though density of ACM decreases, the Brunauer–Emmett–Teller (BET) surface areas of its outer layer and core increase by 1582 times and 42 times, respectively (Fig. 2e). Pore size distribution analysis shows that the gigantic specific surface areas were derived from nanopores with the size of ~0.5 nm which were generated by the reaction between carbon and KOH (Fig. 2f). However, the BET surface area of the core is much smaller than that of the morning glory-like structure for ACM, indicating activation reaction has a greater influence on the morning glory-like structure. Furthermore, the increase of defect density after activation can also be confirmed by the increased Raman intensity ratio I<sub>D</sub>/I<sub>G</sub> of Raman spectrum (Fig. 2e and Fig. S3e, Supporting Information). For example, the I<sub>D</sub>/I<sub>G</sub> of the morning glory-like structure rises from 0.88 to 1.02 after activation. The chemical elements of ACM were investigated by X-ray Photoelectron Spectroscopy (XPS). As shown in Fig. 2h, the ratio of carbon and oxygen atoms in the activated sample is much smaller than that in the unactivated sample, indicating the increased proportion of oxygen atoms (oxygen-containing functional groups). In addition, the C 1s XPS spectrums of activated morning glory-like structure (Fig. 2i) and core (Fig. S3f, Supporting Information) both display markedly the peak of oxygen functional groups C-O-C or OH centered at 186.6 eV. What's more, peak area proportion of C-O-C and OH is larger than unactivated samples. To sum up, activation has two

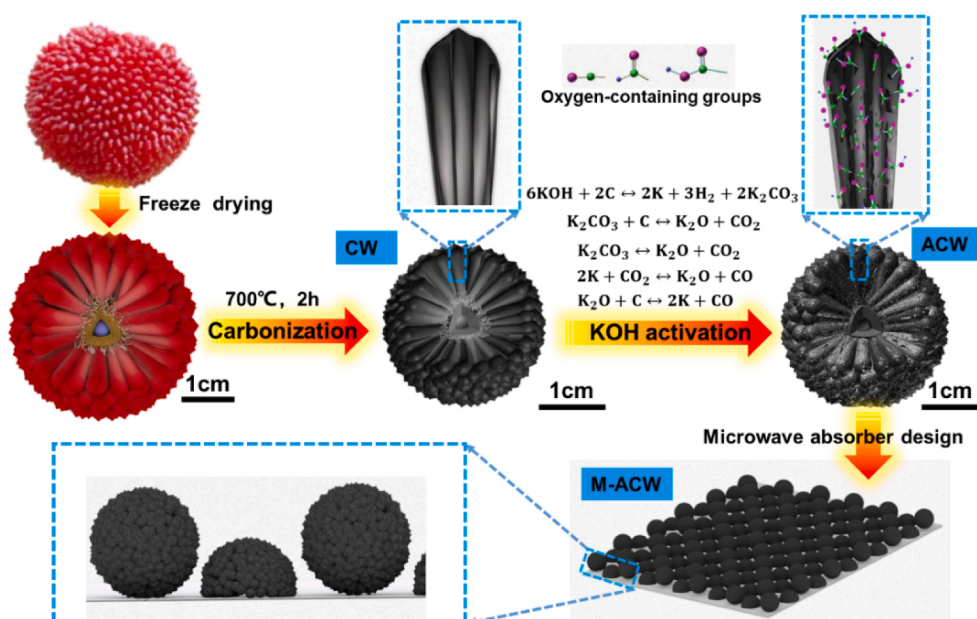
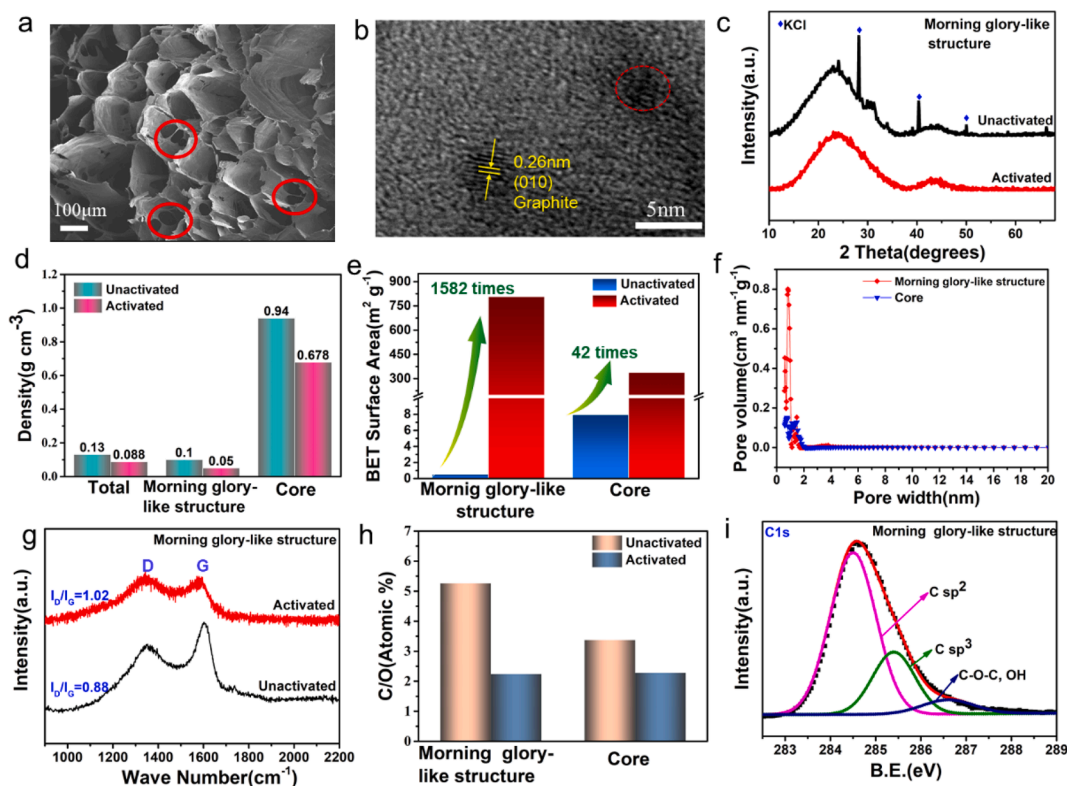


Fig. 1. Schematic of the preparation process and microstructure of M-ACW.



**Fig. 2.** (a) SEM image and (b) TEM image of activated morning glory-like structure. (c) XRD patterns of activated morning glory-like structure, (d) component density and total density before and after activation, (e) BET surface area before and after activation, (f) pore size distribution of different parts after activation, (g) Raman spectra of morning glory-like structure, (h) the ratio of carbon to oxygen obtained by XPS and (i) high-resolution XPS spectra of C 1s of activated morning glory-like structure.

effects on CW: one is to increase BET surface area enormously by producing plenty of micropores, which is beneficial to interface polarization; the other is to boost the ratio of oxygen-containing functional groups, which can enhance the dipole polarization.

To optimize the activation process, we investigated the influence of temperature (600 °C, 650 °C, 700 °C, 750 °C) and KOH concentration (saturated solution, 430 g ml<sup>-1</sup>, 262 g ml<sup>-1</sup>, 56 g ml<sup>-1</sup>) on the EM parameters of the morning glory-like structure. When the activated temperature ranged from 600 to 700 °C, the higher the temperature, the larger the real ( $\epsilon'$ , storage modulus), imaginary parts ( $\epsilon''$ , loss modulus) and dielectric loss tangent values ( $\tan \delta_\epsilon = \epsilon''/\epsilon'$ , which characterizes the

EM wave loss ability), as shown in Fig. 3, Fig. S4 (Supporting Information) and Fig. S5 (Supporting Information). However, when activating temperature exceeds 700 °C, the excessive reaction will lead to the structural damage of the sample. Fig. 3 shows the EM parameters of morning glory-like structure before and after activation at 700 °C. Compared with the CW, the  $\epsilon'$  and  $\epsilon''$  values of the ACW permittivity (Z-axis or Y-axis) were increased several times in the low-frequency field. For instance, even if the KOH concentration is only 56 g L<sup>-1</sup>, the  $\epsilon'$  and  $\epsilon''$  in Z-axis have risen approximately 6 times and 10 times at 2 GHz, respectively. Nevertheless, with the increase of frequency, the influence of activation on dielectric constant decreases (Fig. S6 and Fig. S7,

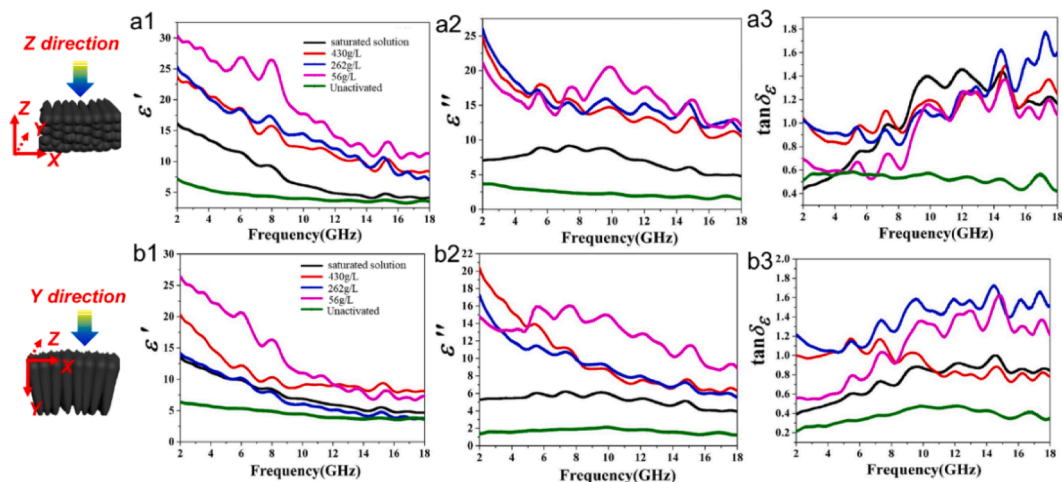


**Fig. 3.** The complex permittivity of morning glory-like structure (before and after activation at 700 °C) in (a1-a3) Z-axis and (b1-b3) Y-axis at 2–18 GHz band: (a1, b1) the real part, (a2, b2) imaginary part, and (a3, b3) dielectric loss tangent.

Supporting Information). The analysis of  $\tan \delta_e$  (Fig. 3a3 and Fig. 3b3) implies that the samples possess the maximum value both in Z-axis and Y-axis when KOH concentration is  $262 \text{ g L}^{-1}$  and activation temperature is  $700 \text{ }^\circ\text{C}$ . It is worth noticing that the low-frequency (2–8 GHz) absorption capacity of the activated samples increases significantly under this activation condition. For example, the  $\epsilon''$  of morning glory-like structure in Z-axis and Y-axis increased by nearly an order of magnitude at low frequency. And the  $\tan \delta_e$  of morning glory-like structure in Z-axis and Y-axis increased 2 and 6 times compared with unactivated ones, respectively. This result meets expectation of improving the low-frequency loss capacity. However, the influences of activation on dielectric properties of core are quite different from outer structure. As indicated in Fig. S8 (Supporting Information), activation process augmented the  $\epsilon'$  of core, meanwhile it reduced its  $\epsilon''$ , resulting in a reduction in  $\delta_e$  at 1–40 GHz.

Next, we will digest the absorption mechanism. Generally, the electromagnetic absorption consists of electrical loss and magnetic loss. As shown in Fig. S9 (Supporting Information), the real component ( $\mu'$ ) is around 1 and the imaginary component ( $\mu''$ ) is 0. Therefore, the magnetic loss mechanism could be excluded. Then the absorption mechanism turns to electrical loss (dielectric and resistance loss). According to Debye theory, the  $\epsilon''$  is defined as follows [26],

$$\epsilon'' = \frac{\epsilon_s - \epsilon_\infty}{1 + \omega^2\tau^2} \omega\tau + \frac{\sigma}{\omega\epsilon_0} = \epsilon_c'' + \epsilon_p'' \quad (1)$$

where  $\epsilon_s$  is the static permittivity,  $\epsilon_\infty$  is the dielectric constant at infinite frequency,  $\omega$  is the angular frequency,  $\tau$  is the relaxation time,  $\sigma$  is the leakage conductivity,  $\epsilon_c''$  and  $\epsilon_p''$  are the contribution of resistance loss (i.e. charge transmission) and dielectric loss (i.e. polarization relaxation) to  $\epsilon''$ , respectively. Based on the Eq. (1), the  $\epsilon_c''$  and  $\epsilon_p''$  can be calculated using the following equations:

$$\epsilon_c'' = \frac{\sigma}{\omega\epsilon_0} \quad (2)$$

$$\epsilon_p'' = \frac{\epsilon_s - \epsilon_\infty}{1 + \omega^2\tau^2} \omega\tau = \epsilon'' - \epsilon_c'' \quad (3)$$

As indicated in Fig. S10 (Supporting Information), the electrical conductivity of the morning glory-like structure increases after activation, which is related to the growing microcrystalline content and oxygen-containing functional groups [27]. Even so, the electrical conductivity values of both the core and morning glory-like structure are only  $10^{-6}$ – $10^{-8} \text{ S m}^{-1}$ . In this case, the  $\epsilon_c''$  calculated by Eq. (2) is so small ( $\sim 10^{-3}$ ) that can be ignored. Therefore, the EM loss of ACW-700 is mainly derived from the  $\epsilon_p''$ . Four kinds of polarization modes, including interfacial, dipole (Debye), atomic and electronic polarization from low-frequency to high-frequency, can occur in a heterogeneous system [8]. Normally, the latter two polarizations exist at a higher frequency ( $\geq 10^{12}$  GHz) [8], so only interfacial and dipole polarization are involved in the measured frequency range. According to Debye theory,  $\epsilon'$  can be written as [26]

$$\epsilon' = \epsilon_\infty + \frac{\epsilon_s - \epsilon_\infty}{1 + \omega^2\tau^2} \quad (4)$$

The relationship between  $\epsilon''$  and  $\epsilon'$  can be deduced from Eqs. (3) and (4) as follows:

$$(\epsilon' - \epsilon_\infty)^2 + (\epsilon'')^2 = (\epsilon_s - \epsilon_\infty)^2 \quad (5)$$

Accordingly, the image of  $\epsilon''$  versus  $\epsilon'$  would be a semicircle, named as *Cole-Cole* semicircle, which indicates a Debye polarization relaxation. When there are multiple relaxation times, the semicircle will take on an arc shape. As shown in Fig. 4b1 and c1, for the morning glory-like structure (both directions), the *Cole-Cole* charts present the approximate linear structure in the range of the 2–18 GHz, which indicates that the dielectric loss mechanism is dominated by interfacial polarization relaxation at the frequency band. Based on Maxwell-Wagner theory

[28,29], interfacial polarization refers to the separation of positive and negative charges of the electron cloud induced by the aggregation of electrons at the interface, as illustrated in Fig. 4a1. The separation is a very slow process. Thus, relaxation of interfacial polarization occurs at relatively low frequencies. As the frequency increases from 18 GHz to 26.5 GHz, the arc structure begins to appear (Fig. 4b2 and c2). When the frequency increases further (26.5–40 GHz), the number of arc shapes grows, indicating the transition process of dielectric loss mechanism from interfacial polarization to Debye polarization. As shown in Fig. 4a2, Debye polarization is essentially the orientation behavior of a dipole in the electric field. The difference of the attractive force to electron cloud between the two atoms connected by a covalent bond causes the electron cloud to lean to one side. Under the action of external electric field, the separation of positive and negative charges generates. Dipole polarization is a relatively fast process, so dipole polarization relaxation occurs at higher frequencies. According to the effective medium theory, the activation process results in a greatly reduced carbon density (Fig. 2d), which leads to a decrease in permittivity. On the other hand, the increment of BET surface area (Fig. 2e) significantly boosts the interface polarization loss at low frequency. As such, there is a balance between the two (surface area increases versus density decreases). And the value of the permittivity is ultimately determined by the synergistic effect of the two. For the morning glory-like structure, the increment of dielectric loss on account of increased specific surface area outstrips the decrement caused by the reduced density at 2–18 GHz. Therefore, the permittivity increases dramatically in this frequency band. However, at higher frequency (18–40 GHz), the increase of dipole polarization relaxation has less influence on the permittivity, leading to a smaller increment in permittivity. As for the core structure, within the whole test frequency band, some arc shapes were observed in the *Cole-Cole* diagram (Fig. S11, Supporting Information), showing that the dipole polarization plays the dominant role in the dielectric loss. Although the number of dipoles increases after activation, the reduced dielectric loss due to the decrease of carbon medium cannot be compensated by the increase of the additional dipole polarization relaxation, which leads to the  $\delta_e$  decreases slightly after activation. In conclusion, the results provide a new idea for the active regulation of the EM loss capacity of non-magnetic materials. Firstly, the loss mechanism of materials should be determined, and then tune permittivity according to the main loss mechanism. For example, if  $\epsilon_c''$  is dominant, the  $\epsilon''$  can be improved by increasing electrical conductivity. If the interfacial polarization is the main factor, the specific surface area should be increased by etching or activation to control the  $\epsilon''$ . In addition, when the dipole polarization relaxation is the main loss mechanism, doping or other methods to increase the dipole content may be a better choice to increase permittivity. Herein, the results proved that the specific surface area and dielectric loss properties could be greatly increased by KOH activation, which might provide researchers an inspiration to solve the problem of low-frequency MA.

The ACW was assembled into a MA array according to a certain period, and the RL was measured by the arc method (See Fig. S12, Supporting Information). As indicated in Fig. 5 a, compared with the sample before activation [24], when the period of ACW array is 28 mm, the low-frequency MA performance was dramatically improved. There is a strong absorption peak of  $-43 \text{ dB}$  at 1–2.5 GHz, which benefits from the improvement of dielectric loss capacity. However, when the period value decreases (the number of samples increases), the effective dielectric constant increases, resulting in the deterioration of impedance matching between air and sample. Instead, the MA performance is reduced (Fig. S13a1-a3, Supporting Information).

In order to address the contradiction between EM loss and impedance matching, structural design was carried out. As shown in Fig. S12 (Supporting Information), the whole ACM ball and the hemisphere were cross-arranged to construct a “metamaterial”, M-ACW. This special structure makes the effective dielectric constant of the lower half layer greater than that of the upper half layer, thus generating gradient

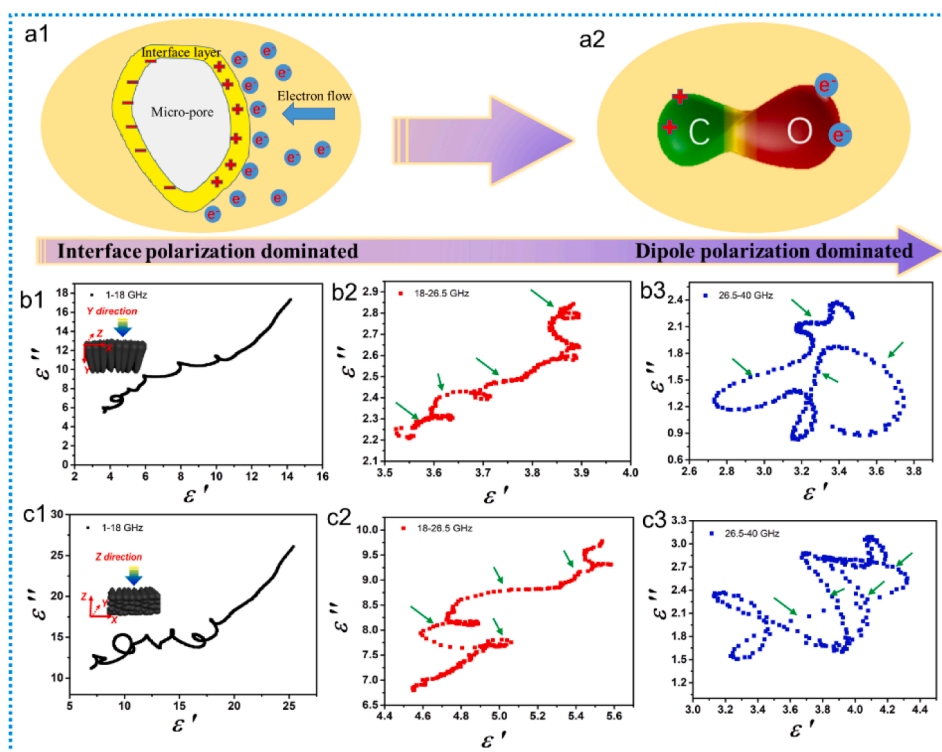


Fig. 4. The schematic diagram of (a1) interfacial polarization and (a2) dipole polarization, the Cole-Cole plot of morning glory-like structure after activation in (b1-b3) Y-axis and (c1-c3) Z-axis at 1–40 GHz.

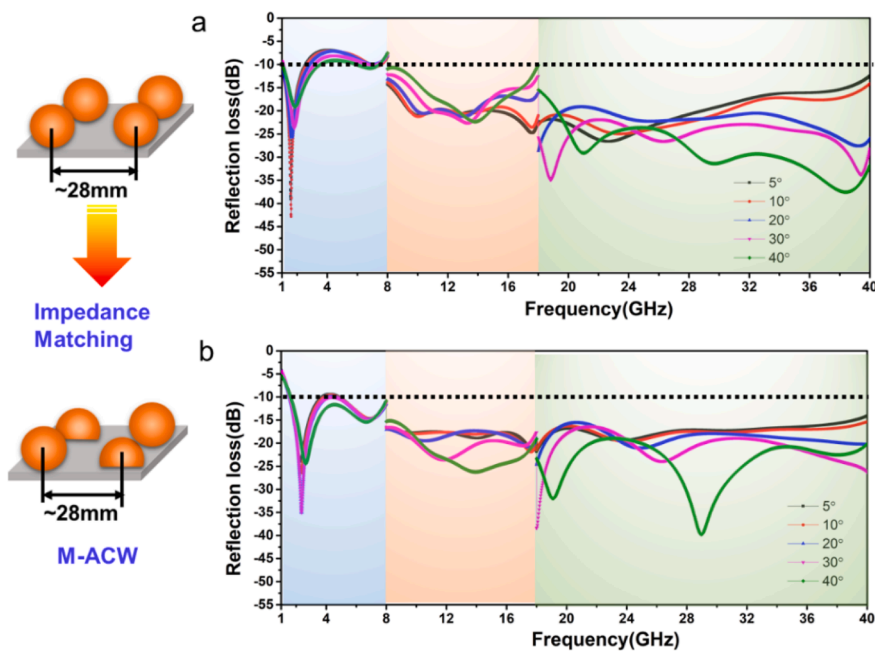


Fig. 5. The measured RL curves (1–40 GHz) of activated ACW array (a) and M-ACW (b).

impedance and realizing better impedance matching. Therefore, as demonstrated in Fig. 5b, obviously, the MA is further improved and shows four advantages. Firstly, M-ACW reveals excellent low-frequency MA performance, especially in the 1–4 GHz that is particularly difficult to achieve MA, and the maximum RL can reach  $-35.1$  dB at 2.4 GHz. The absorption ratio of the ACW array and the M-ACW were calculated, as shown in Fig. S14. Compared with ACW array (absorption ratio is more than 80%), the absorption ratio (more than 90% at 1.5–8 GHz) of

the M-ACW is significantly increased at low frequency. And the absorption rate of the two samples both can reach more than 98% at high frequency (8–40 GHz). In addition, the absorption peak can be moved to a lower frequency through adjusting the periodic parameters, so as to achieve an effective ultra-low frequency MA of 1–3 GHz (Fig. S15, Supporting Information). Secondly, The M-ACW can realize ultrabroad band MA. The RL is less than  $-10$  dB in the frequency range from 1.5 GHz to 40 GHz, covering 98.7% of the whole test range. The MA

properties of high-performance absorbers reported in recent years, including pure carbon materials [30–33], carbon/magnetic composite materials [19–23], multi-scale carbonized biomass [7–10,34–38], and structural absorber [12–18], are summarized in Fig. 6. In comparison with previous results, M-ACW shows incomparable advantages in low-frequency as well as broadband MA. Thirdly, since there are no magnetic materials and other resin materials introduced, the apparent body density of M-ACW is only  $0.019 \text{ g cm}^{-3}$ . Lastly, the spherical structure gives it unique angular insensitivity. When the incident angle changes from  $5^\circ$  to  $40^\circ$ , it still maintain excellent MA performance, which means it can deal with electromagnetic wave pollution from multiple angles.

The outstanding MA performances were explained by its unique multi-scale structure and various EM loss mechanisms, as illustrated schematically in Fig. 7. i) At microscopic scale (nm scale), as shown in Fig. 7a, the activation results in increasing electrical conductivity, which contributes to the improvement of resistance loss ability. More oxygen-containing functional groups were introduced during activation, promoting polarization relaxation loss of dipoles. More importantly, the BET result indicates that the plenty of interface were introduced thus enhanced the interfacial polarization relaxation loss at low frequency. ii) At mesoscopic scale ( $\mu\text{m}$  scale), as shown in Fig. 7b, hollow tubular structures with diameters ranging from several microns to hundreds of microns and hollow core structures play the role of resonators. In this case, EM waves were reflected and absorbed in the resonator repeatedly. Both multiple reflection and absorption process enhanced the intensity of MA. iii) At macroscopic scale (mm-cm scale), the unique structural design facilitates impedance matching (Fig. 7c). According to the theory of effective medium [39], there is no doubt that the relationship between the equivalent permittivity of the upper ( $\epsilon_{eq1}$ ) and bottom layers ( $\epsilon_{eq2}$ ) exists:  $\epsilon_{eq1} < \epsilon_{eq2}$ . The  $\epsilon_{eq1}$  is closer to that of air. This gradience makes the impedance of M-ACW match better, which is the basis of MA. Moreover, this method provides a totally new idea to realize impedance matching when designing the lower-frequency MA materials. These three aspects contribute the low frequency and broad band absorption.

### 3. Conclusion

In summary, the carbonized waxberry could be successfully activated by KOH solution. After activation, the BET surface area of the outer structure of waxberry is increased by 1582 times, which greatly boosts the EM loss due to interfacial polarization. As a result, the  $\epsilon''$  of morning glory-like structure increased by nearly an order of magnitude at low frequency, and the permittivity can be effectively tuned by activation temperature and KOH concentration. The macroscopic periodic metamaterial based on activated and carbonized waxberry demonstrates ultralow-frequency and ultrabroad band MA property with more than 90% absorption ( $\text{RL} < -10 \text{ dB}$ ) in the frequency range of 1–40 GHz. In addition, the absorber still maintains the good MA performance when the incident angle changes from  $5^\circ$  to  $40^\circ$ . These are attributed to impedance gradient structure and multi-scale EM loss mechanism.

### 4. Experimental section

#### 4.1. Materials synthesis

The CW was prepared using the method we reported previously [24]. Then, the resultant CW was placed into KOH solutions with different concentrations (saturated solution,  $430 \text{ g ml}^{-1}$ ,  $262 \text{ g ml}^{-1}$ ,  $56 \text{ g ml}^{-1}$ ) and KOH solutions were immersed into CW by vacuum assisted method. After repeated perfusion for several times, the CWs were dried at  $60^\circ \text{C}$  for 48 h. Afterward, the dried CW/KOH samples were activated at  $600^\circ \text{C}$ ,  $650^\circ \text{C}$ ,  $700^\circ \text{C}$  and  $750^\circ \text{C}$  for 2 h in argon gas atmosphere, respectively. The heating rate was  $5^\circ \text{C min}^{-1}$ . After cooled down to room temperature in argon, the activated CW (ACW) sample were washed repeatedly using deionized water till the pH value is 7. Subsequently, the ACW were dried at  $60^\circ \text{C}$  for more than 48 h. The hemispherical ACW were obtained by cutting the whole frozen waxberry mechanically at the beginning and then treating it using the same method (as shown in Fig. S2, Supporting Information). The M-ACW was prepared by putting the whole and hemisphere ACW periodically on an acrylic plate ( $300 \times 300 \text{ mm}$  in length and 2 mm in thickness) with some holes (for fixing the samples). The total numbers of ACW for an M-ACW could be 121, 144, or 169 (the corresponding period parameters are 28 mm, 25.5 mm, and 23 mm, respectively).

#### 4.2. Characterization and measurement

The microstructure of ACW was characterized by Scanning Electron Microscopy (SEM, Carl Zeiss, supra55) and Transmission Electron Microscopy (TEM, JEM 2100). XRD patterns were acquired by using a X-ray diffractometer (Ultima IV) under CuK radiation (wavelength is  $0.154 \text{ nm}$ ) at a scanning rate of  $2^\circ \text{ min}^{-1}$ , voltage of 40 kV, and current of 40 mA. Raman spectra were obtained by Raman spectrometer (Renishaw, inVia-Reflex). The chemical states of samples were examined by X-ray Photoelectron Spectroscopy (ESCALAB 250Xi). The distribution of K was determined by the map scanning of Energy Dispersive Spectrometer (Oxford Instrument). The specific surface area and pore structure of samples were characterized by automatic gas-adsorption instrument (Quantachrome, AUTOSORB IQ). All samples were degassed at  $200^\circ \text{C}$  for 12 h under vacuum condition before the measurement. The specific surface area was calculated by the multiple points Brunauer–Emmett–Teller (BET) method and the pore size distribution was analyzed based on Density Functional Theory (DFT). The apparent bulk density of M-ACW was calculated by:

$$\frac{m_{total}}{30 \times 30 \times 2}$$

where  $m_{total}$  is total mass of all samples, and the “ $30 \times 30 \times 2$ ” is the apparent volume of the metamaterial. The electrical conductivities of CW and ACW-700 were measured using a SourceMeter instrument (KEITHLEY, 2460), and the testing samples were prepared by the

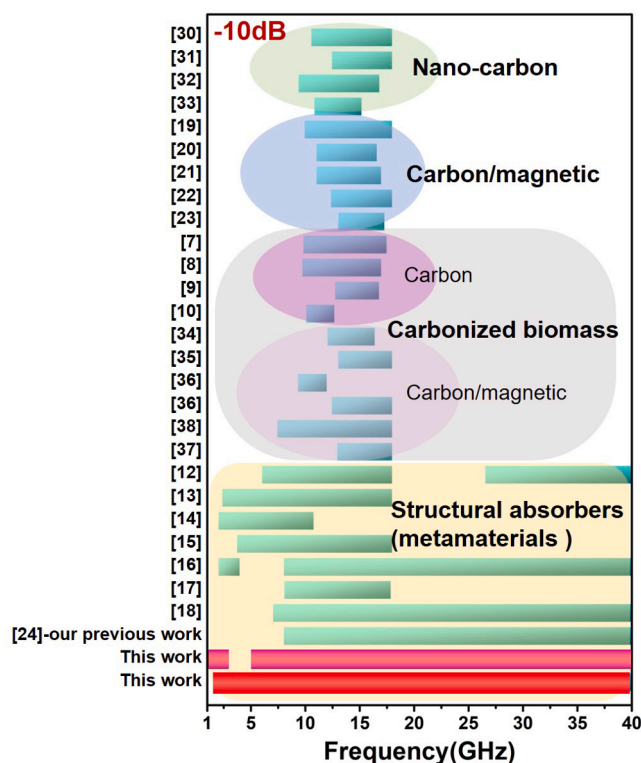


Fig. 6. Comparison of bandwidths with over 90% absorption ( $\text{RL} \leq -10 \text{ dB}$ ) between M-ACW and as-reported EM wave absorbers.

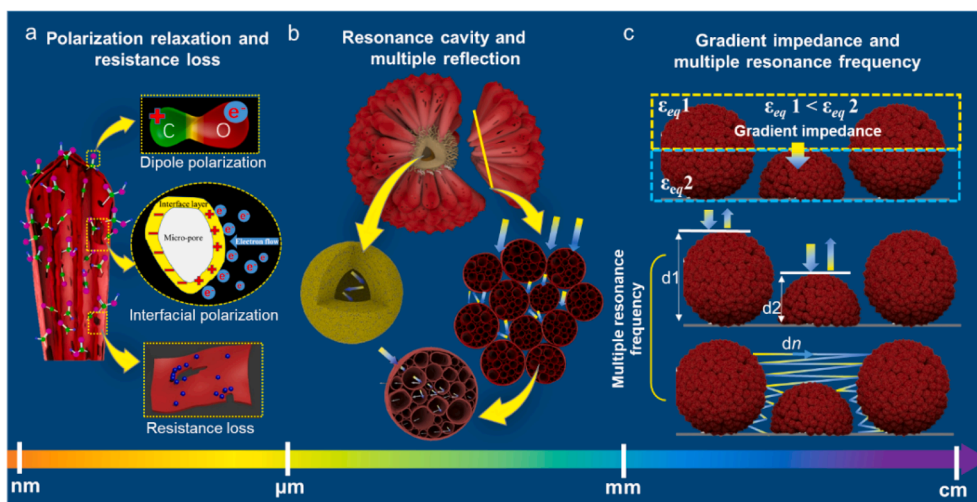


Fig. 7. Schematic diagram of the multi-scale loss mechanism of M-ACW.

method of producing the EM parameter testing sample.

#### 4.3. EM parameters and RL test

Similar to our previous work [24], the electromagnetic parameters were measured using an Agilent Technologies N5222A network analyzer. Briefly, the complex permittivity in the frequency range of 1–18 GHz were obtained by the coaxial-line method method (outer diameter is 7.0 mm and an inner diameter is 3.0 mm), and were measured at 18–26.5 GHz and 26.5–40 GHz through the waveguide method (the sizes are  $10.668 \times 4.318$  mm and  $7.112 \times 3.556$  mm, respectively). The two methods are based on the principle of transmission/reflection method. For the measurement, the outer morning glory-like structure was immersed into the melted paraffin (supporting material) by vacuum-assisted perfusion. After paraffin injection, the sample was cut into slices with a certain thickness and put into a stamping die (see Fig. S16a) to press out a ring with a diameter of 7 mm (The first stamping). The ring is then placed in a secondary stamping mould (see Fig. S16b), and a cylinder with a diameter of 3 mm is punched from the center (The second stamping) to obtain a concentric ring sample. It should be noted that each stamping should ensure that the upper and lower sides of the sample are pressed tightly. However, samples of ball-like core were ground into powders and then uniformly mixed into paraffin with a mass ratio of 1:0.92 (density of the carbon powders in composites is close to the original density of the core wall). The RL was measured in situ by Arc method, as illustrated in Fig. S12 (Supporting Information). The M-ACW was put on a standard metal board located in the middle of microwave darkroom. To avoid the edge effect, different antennas were employed in frequency ranges of 1–8 GHz, 8–18 GHz and 18–40 GHz, respectively. The incident angles of EM waves were adjusted to  $5^\circ$ ,  $10^\circ$ ,  $20^\circ$ ,  $30^\circ$ , and  $40^\circ$  so as to analyze the angle-independent properties of samples.

#### Declaration of Competing Interest

The authors declare that they have no known competing financial interests or personal relationships that could have appeared to influence the work reported in this paper.

#### Acknowledgements

This manuscript was financially sponsored by National Natural Science Foundation of China (NSFC, Grant No. 51772063, No. 11734007 and No. 91850101) and Shenzhen Science and Technology Program (Grant No. KQTD2016112814303055).

#### Appendix A. Supplementary data

Supplementary data to this article can be found online at <https://doi.org/10.1016/j.cej.2021.130142>.

#### References

- [1] S. Gupta, N.-H. Tai, *Carbon* 152 (2019) 159.
- [2] Q. Li, Z. Zhang, L. Qi, Q. Liao, Z. Kang, Y. Zhang, *Adv. Sci. (Weinh)* 6 (2019) 1801057.
- [3] M. Bakur, Ş. Dalgaç, E. Ünal, F. Karadağ, M. Demirci, A.S. Köksal, O. Akgöl, M. Karaaslan, *Water Air Soil Pollut.* 230 (2019) 304.
- [4] Ş. Dalgaç, F. Karadağ, M. Bakur, O. Akgöl, E. Ünal, M. Karaaslan, *Trans. Inst. Meas. Control* (2020), 0142331220976104.
- [5] S. Kacin, M. Ozturk, U.K. Sevim, B.A. Mert, Z. Ozer, O. Akgöl, E. Unal, M. Karaaslan, *Nat. Hazards* (2021) 1.
- [6] C.M. Watts, X. Liu, W.J. Padilla, *Adv. Mater.* 24 (2012) OP98.
- [7] J. Xi, E. Zhou, Y. Liu, W. Gao, J. Ying, Z. Chen, C. Gao, *Carbon* 124 (2017) 492.
- [8] Z. Wu, K. Tian, T. Huang, W. Hu, F. Xie, J. Wang, M. Su, L. Li, *ACS Appl. Mater. Interfaces* 10 (2018) 11108.
- [9] C. Wang, Y. Ding, Y. Yuan, X. He, S. Wu, S. Hu, M. Zou, W. Zhao, L. Yang, A. Cao, Y. Li, *J. Mater. Chem. C* 3 (2015) 11893.
- [10] X. Qiu, L. Wang, H. Zhu, Y. Guan, Q. Zhang, *Nanoscale* 9 (2017) 7408.
- [11] T. Kim, J.Y. Bae, N. Lee, H.H. Cho, *Adv. Funct. Mater.* 29 (2019) 1807319.
- [12] Y. Zhang, Y. Huang, T. Zhang, H. Chang, P. Xiao, H. Chen, Z. Huang, Y. Chen, *Adv. Mater.* 27 (2015) 2049.
- [13] M. Li, B. Muneer, Z. Yi, Q. Zhu, *Adv. Opt. Mater.* 6 (2018) 1701238.
- [14] K. Pan, T. Leng, J. Song, C. Ji, J. Zhang, J. Li, K.S. Novoselov, Z. Hu, *Carbon* 160 (2020) 307.
- [15] Y. Zhang, Y. Huang, H. Chen, Z. Huang, Y. Yang, P. Xiao, Y. Zhou, Y. Chen, *Carbon* 105 (2016) 438.
- [16] Y. Huang, X. Yuan, M. Chen, W.-L. Song, J. Chen, Q. Fan, L. Tang, D. Fang, A.C. S. Appl. Mater. Interfaces 10 (2018) 44731.
- [17] L.X. Huang, Y.P. Duan, X.H. Dai, Y.S. Zeng, G.J. Ma, Y. Liu, S.H. Gao, W.P. Zhang, *Small* 15 (2019) 1902730.
- [18] W.L. Song, Z. Zhou, L.C. Wang, X.D. Cheng, M. Chen, R. He, H. Chen, Y. Yang, D. Fang, *ACS Appl. Mater. Interfaces* 9 (2017) 43179.
- [19] Q.H. Liu, Q. Cao, H. Bi, C.Y. Liang, K.P. Yuan, W. She, Y.J. Yang, R.C. Che, *Adv. Mater.* 28 (2016) 486.
- [20] X.J. Zhang, J.Q. Zhu, P.G. Yin, A.P. Guo, A.P. Huang, L. Guo, G.S. Wang, *Adv. Funct. Mater.* 28 (2018) 1800761.
- [21] J.J. Ding, L. Wang, Y.H. Zhao, L.S. Xing, X.F. Yu, G.Y. Chen, J. Zhang, R.C. Che, *Small* 15 (2019) 1902885.
- [22] L. Yan, M. Zhang, S. Zhao, T. Sun, B. Zhang, M. Cao, Y. Qin, *Chem. Eng. J.* 382 (2020), 122860.
- [23] X. Wang, F. Pan, Z. Xiang, Q. Zeng, K. Pei, R. Che, W. Lu, *Carbon* 157 (2020) 130.
- [24] X. Sun, M. Yang, S. Yang, S. Wang, W. Yin, R. Che, Y. Li, *Small* 15 (2019) 1902974.
- [25] A.B. Bourlino, V. Georgakilas, R. Zboril, D. Jancik, M.A. Karakassides, A. Stassinopoulos, D. Anglos, E.P. Giannelis, *J. Fluorine Chem.* 129 (2008) 720.
- [26] M. Cao, X. Wang, W. Cao, X. Fang, B. Wen, J. Yuan, *Small* 14 (2018) 1800987.
- [27] S. Mrozowski, *Phys. Rev.* 85 (1952) 609.
- [28] K.W. Wagner, *Arch. Elektrotech.* 2 (1914) 378.
- [29] J.C. Maxwell, *A treatise on electricity and magnetism*, 3rd ed., Clarendon Press, Oxford, 1881.
- [30] X. Zhang, X. Wang, F. Meng, J. Chen, S. Du, *Carbon* 154 (2019) 115.
- [31] C. Chen, J. Xi, E. Zhou, L. Peng, Z. Chen, C. Gao, *Nano-Micro Letters* 10 (2017) 26.

- [32] W. Liu, H. Li, Q. Zeng, H. Duan, Y. Guo, X. Liu, C. Sun, H. Liu, *J. Mater. Chem. A* 3 (2015) 3739.
- [33] H. Sun, R. Che, X. You, Y. Jiang, Z. Yang, J. Deng, L. Qiu, H. Peng, *Adv. Mater.* 26 (2014) 8120.
- [34] H. Zhao, Y. Cheng, J. Ma, Y. Zhang, G. Ji, Y. Du, *Chem. Eng. J.* 339 (2018) 432.
- [35] H. Zhao, Y. Cheng, H. Lv, G. Ji, Y. Du, *Carbon* 142 (2019) 245.
- [36] J. Fang, Y. Shang, Z. Chen, W. Wei, Y. Hu, X. Yue, Z. Jiang, *J. Mater. Chem. C* 5 (2017) 4695.
- [37] Z.C. Wu, K. Pei, L.S. Xing, X.F. Yu, W.B. You, R.C. Che, *Adv. Funct. Mater.* 29 (2019) 1901448.
- [38] L. Wang, X. Li, Q. Li, X.F. Yu, Y.H. Zhao, J. Zhang, M. Wang, R.C. Che, *Small* 15 (2019) 1900900.
- [39] J.C. Garnett, Maxwell, *Philos. Trans. R. Soc. A* 205 (1906) 237.